Compression Strength of Composite Primary Structural Components

Semiannual Status Report

Eric R. Johnson
Principal Investigator

Performance Period: November 1, 1992 to April 30, 1993

NASA Grant NAG-1-537

Aerospace and Ocean Engineering Department
Virginia Polytechnic Institute and State University
Blacksburg, Virginia 24061-0203

October, 1993

Technical Monitor: Dr. James H. Starnes, Jr., Head
Aircraft Structures Branch
National Aeronautics and Space Administration
Langley Research Center
Hampton, Virginia 23681-0001

INTRODUCTION

Two projects are summarized in this report. The first project is entitled *Stiffener Crippling Initiated by Delamination*, and the second is entitled *Pressure Pillowing of an Orthogonally Stiffened Cylindrical Shell.*

The write-up in the "Research Accomplished" section for the first project is the text of a conference paper that appeared in

- *Mechanics of Composite Materials—Nonlinear Effects*, edited by M. W. Hyer, AMD-Vol. 159, American Society of Mechanical Engineers, New York, NY, 1993, pp. 19-28.

This conference paper was submitted March 1, 1993 to the editor. The papers in this ASME volume were presented at the 1st Joint Mechanics Meeting of ASME • ASCE • SES – MEET'N'93, Charlottesville, Virginia, June 6 -9, 1993.

The write-up in the "Research Accomplished" section for the second project is based on the presentation (presenter in boldface font)

- **Johnson, Eric R.**, and Rastogi, Naveen, "Interacting Loads in an Orthogonally Stiffened Composite Cylindrical Shell," presented in Session 25 — Work-in-Progress 1, at *The 34th AIAA/ASME/ASCE/AHS/ASC Structures, Structural Dynamics and Materials Conference*, April 19-21, 1993, Hyatt Regency, LaJolla, California

RESEARCH ACCOMPLISHED

I. Stiffener Crippling Initiated by Delamination

Background and objective

Graphite-epoxy stiffeners tested in compression (Bonanni, Johnson, and Starnes, 1991) showed evidence of failure initiation in postbuckling by delamination at the free edges of the flanges. This mode of failure initiation occurred in *I*- and *J*-section specimens with flange width to thickness ratios in the range from ten to twenty. The analyses conducted in the Bonanni study modeled the stiffeners as a branched shell using the STAGS computer code. Since shell theories are based on plane stress and neglect through-the-thickness stress components, failure initiated by interlaminar stresses at the free edges of the flanges due to bending in postbuckling could not be studied with the STAGS model.

The objective of this project is to develop a computational model of the stiffener specimens that includes the capability to predict the interlaminar stress response at the flange free edge in postbuckling.

Finite Element Analysis

Variable complexity modeling

The analyses were performed using the COMET (Stewart, 1989) structural analysis software system. A variable complexity modeling strategy is employed which first captures the overall geometrically nonlinear response of the specimen to its failure initiation load using all shell elements in the model, and second changes the complexity of the model to include a sub-domain of solid elements at the free edge of a flange from which interlaminar stresses can be computed. The branched shell model of the stiffener is shown in Fig. 1, and the complex model is shown in Fig. 2. The displacement field of the shell model is used to estimate the initial guess of displacement field for the complex model in Newton's method at the failure load. Thus, the complex model only goes through one sequence of Newton's iterations at the final load step, rather than using the complex model through all the intermediate load steps. This strategy keeps problem size small relative to a fully nonlinear three-dimensional model of the I-stiffener. A fully three-dimensional model would tax available computer resources and is not warranted based on the localized nature of the three-dimensional effects.

Shell, transition, and solid elements

The shell element used from the COMET library is denoted EX97, and it is an assumed natural strain element with nine nodes and five degrees of freedom per node. The degrees of freedom are the three displacements of the reference surface and the two rotations of the normal to the reference surface. (No drilling degree of freedom is included.) Element EX97 can be used for flat plate analysis, which is the situation for the web and flanges of the I-stiffener. The solid element is the standard twenty-node serendipity brick with three displacement degrees of freedom per node. This brick element is denoted as BR20 in the COMET library. Since the shell and brick elements are kinematically incompatible, transition elements are required to interface between them. The two transition elements TR12 and TR15 in COMET are employed (Dávila, 1993). Element TR12 has twelve nodes, five of which have the five shell degrees of freedom compatible with EX97, and the remaining seven nodes have the three displacement degrees of freedom compatible with BR20. Element TR15 has fifteen nodes, three of which have the five shell degrees of freedom and the remaining twelve nodes have the three solid element degrees of freedom. These elements are particularly useful for laminate modeling since one shell element can be connected to several TR12 or TR15 elements stacked through the thickness of the laminate. That is, *the nodes of the transition element that have the five shell degrees of freedom do not have to lie on the boundary of the element.* Element TR12 is used at two of the corners of the sub-domain since it is compatible on two of its adjacent faces with EX97, whereas element TR15 has one shell compatible face and is used along three of the edges of the sub-domain. BR20 elements fill the interior of the sub-domain and the interior part of the fourth edge, which coincides with the traction-free edge for the flange.

The geometrically nonlinear analysis is based on the total Lagrangian formulation, and the fully nonlinear Green-Lagrange strain-displacement relations are employed for the solid and transition elements. A modified Newton's method is used to solve the nonlinear equations, and an arc-length strategy is used for continuation along the nonlinear equilibrium path in load-displacement space.

Modeling Specimens I2 and I10

Analyses of specimens I2 and I10 from the experimental study by Bonanni, et al. (1991) were conducted using the methodology discussed above. Nomenclature for the cross-sectional dimen-

sions is shown in Fig. 3., and measured dimensional data used in the analysis of each specimen are listed in Table 1. Also, the buckling load P_{cr} and crippling load P_{cc} from the experiment are listed in this table. The specimens were fabricated from AS4/3502 graphite/epoxy unidirectional tape and material properties used are listed in Table 2. The wall laminate for specimen I2 was an eight ply layup with a stacking sequence of $[\pm 45/0/90]_S$, where a zero degree ply designates fibers parallel to the x-axis in Fig. 1. The laminate for specimen I10 is sixteen plies with $[\pm 45/0/90]_{2S}$ stacking sequence. However, the fabrication procedure for the I-specimens resulted in two diagonally opposite flanges having unsymmetrical stacking sequences. For the eight-ply wall the unsymmetrical stacking sequence is $[\pm 45/0/90_2/0/\pm 45]_T$, and for the sixteen-ply wall the unsymmetrical stacking sequence is $[(\pm 45/0/90)_2/(90/0/\pm 45)_2]_T$. About one inch of the stiffener at each end was supported in an aluminum potting compound as part of the end fixture support. The unsupported length of specimen outside the potted ends is denoted as the gage length l_g, and the total length of the specimen is denoted by L. Clamped end boundary conditions were imposed at each end ($x = 0$ and $x = L$) in the finite element models, as well as prescribing the out-of-plane displacement for the elements contained in the potted ends to vanish.

Credibility of the branched shell model for each stiffener was based on comparing the finite element analysis to the experiment on the load-end shortening response plot. This plot for specimen I10 is shown in Fig. 4. (The correlation between analysis and experiment for specimen I2 was better than shown for I10 in Fig. 4.) To achieve the good agreement between analysis and experiment as shown in Fig. 4, we determined by trial and error selected material stiffnesses to closely match the prebuckling stiffness and buckling load of the specimens in the experiment. The unidirectional filler material in each web-flange junction shown in Fig. 3 was modeled as a beam-column and the modulus selected for this material is listed in Table 2. In addition, the fiber direction modulus for AS4/3502 was changed from its nominal value of 18.5 Msi, and the value selected for each specimen is listed in Table 1.

There were 7,175 degrees of freedom for the unrestrained branched shell model of specimen I2, and 5,945 degrees of freedom for the unrestrained branched shell model of specimen I10. The complex model for specimen I2 had 168 BR20 elements and 10,325 degrees of freedom, and the complex model for specimen I10 had 192 BR20 elements and 9,005 degrees of freedom. The sub-domain of solid elements was about one inch in length (x-direction in Fig. 1) and its position along the flange could be varied. The width (y-direction) of the sub-domain was 0.30 inches for specimen I2, or $4.4t$ where t is the laminate's thickness. The width was 0.20 inches, or $2.4t$, for specimen I10. Note that coordinate $y = 0$ at the free edge. The number of solid elements through the thickness of the flange for specimens I2 and I10 is shown in Fig. 5. When one element is used to span more than one ply, then effective three-dimensional stiffnesses for this sublaminate are determined by a homogenization procedure contained in the LAU processor of COMET. This homogenization procedure is similar to one presented by Sun and Li (1988).

Delamination Index

The intensity of the interlaminar stresses was quantified by the dimensionless index F, defined by

$$F = \left(\frac{\tau_{zz}}{Z^T}\right)^2 + \left(\frac{\tau_{zx}}{Z^{S1}}\right)^2 + \left(\frac{\tau_{zy}}{Z^{S2}}\right)^2 \qquad \tau_{zz} \geq 0$$
$$= \left(\frac{\tau_{zx}}{Z^{S1}}\right)^2 + \left(\frac{\tau_{zy}}{Z^{S2}}\right)^2 \qquad \tau_{zz} < 0 \tag{1}$$

where τ_{zz} is the interlaminar normal stress (positive in tension), τ_{zx} is the interlaminar shear stress tangent to the free edge, and τ_{zy} is the interlaminar shear stress normal to the free edge. The interlaminar strengths Z^T, Z^{S1}, and Z^{S2} used for the AS4/3502 graphite/epoxy material system are given in Table 2. Since this data is difficult to measure, the interlaminar tensile strength is assumed equal to the lamina in-plane transverse tensile strength ($Z^T = Y_t$), and the interlaminar shear strengths are assumed equal to the lamina in-plane shear strength ($Z^{S1} = Z^{S2} = S$). Only tensile interlaminar normal stresses are assumed to contribute to the delamination index. The form of Eq. (1) suggests that values of $F \geq 1$ define an interlaminar strength failure. However, it is likely that an elasticity solution to this effective modulus model of the laminate would have a stress singularity at the free edge, and this implies a criterion based on stress magnitude is meaningless. Thus, we prefer to use Eq. (1) as an indicator of the severity of the interlaminar stress state for this approximate solution (finite element model).

Equation (1) is similar to the quadratic equations used for the prediction of delamination initiation at the straight free edge in tensile/compression coupons by Brewer and Lagace (1988) and by Kim and Soni (1986). These delamination criteria use average values of the interlaminar stresses rather than point-wise values. Average values of the interlaminar stresses are obtained by integrating the interlaminar distributions over a critical length in the interface, and this length is hypothesized to be one ply thickness or a material parameter. Also, the manner in which compressive interlaminar normal stress contributes to these quadratic stress criteria are different than what is shown in Eq. (1).

Results And Discussion

The distribution of the delamination index for specimen I10 is plotted over the 0/90 interface in Fig. 6 at a load near failure ($P/P_{cc} = 1.03$). This 0/90 interface is near the mid-plane of the laminate and is labeled number 3 in Fig. 5(b). The longitudinal position of the sub-domain of solid elements is 1.6 in. $< x <$ 2.4 in. This location corresponds to the neighborhood of the inflection point in the plot of the out-of-plane displacement of the flange along its free edge from the shell solution, $w(x, 0)$, as shown in Fig. 7. The largest magnitude of F in Fig. 6 is 0.73 ($= F_{max}$) and it occurs at the free edge where $y = 0$ (actually it occurs at the Gauss point closest to the free edge) and at $x = 2.03$ in. This data is also itemized in Table 3. The largest contributor to F_{max} is the interlaminar shear stress τ_{zx} as shown in Table 3, and the interlaminar normal stress is compressive at this location. The distributions of τ_{zx} and τ_{zz} in the 0/90 interface are shown in Figs. 8 and 9, respectively. Other longitudinal positions for the sub-domain were investigated, but the neighborhood of the inflection point resulted in the largest value of F found. For instance, the maximum value of F in the neighborhood of the buckle crest is 0.02 (see Table 3).

For specimen I2 at a load near failure ($P/P_{cc} = 1.02$) $F_{max} = 0.4$, and it occurs at $x = 6.24$ in., y

= 0, and in the 4th interface (90/0) shown in Fig. 5(a). The longitudinal position where F_{max} occurs is again near an inflection point of *w(x,0)* from the shell solution. The largest contributor to F_{max} is the interlaminar shear stress τ_{zx}, and τ_{zz} is compressive. Longitudinal positions near the buckle crest and node point were investigated as well, and these results are listed in Table 3.

In both specimens the severest interlaminar stress intensity is dominated by the shear stress component (τ_{zx}) tangent to the free edge. The axial location along the free edge of the flange where F_{max} occurs is near the location where the transverse shear resultant Q_x from the shell solution is a relative maximum. Refer to Fig. 7. Relative maxima of Q_x are near the inflection points of *w(x,0)*. Thus, τ_{zx} attains a large value where its corresponding shell resultant Q_x is large, which is what one would expect. For postbuckled laminated plates having edge support all around Starnes and Rouse (1981), and Davies et al. (1986), have also observed that the transverse shear resultant, or the shear stress component tangent to the edge, causes failure at the intersection nodal line and the unloaded edge. The interlaminar normal stress component (τ_{zz}) is compressive where F_{max} occurs, and its magnitude (Table 3) is small; i.e., the square of the ratio of τ_{zz} to the transverse compression strength of a lamina, which is about 30 ksi for AS4/3502, is small compared to the shear terms in Eq. (1). Thus, for the analyses of specimens I2 and I10 it appears unlikely that the compression values of τ_{zz} would contribute much to delamination initiation.

We expect the maximum value of the index F to exceed unity if delamination initiation is predicted. Failure initiation for specimen I10 was observed in the experiment to be by free edge delamination, and an $F_{max} = 0.73$ at $P = 1.03\ P_{cc}$ from the analysis does not correlate with this observation. Failure initiation for I2 was by a material compressive strength failure in the corner, and an $F_{max} = 0.4$ at $P = 1.02\ P_{cc}$ is consistent with this observed mode in the sense that delamination initiation is unlikely.

The discrepancy between the analysis and experiment for specimen I10 may be due to the omission of modeling progressive failures in the laminate. Strain gage data indicated a damage event at 18, 750 lbs ($P/P_{cr} = 1.11$, $P/P_{cc} = 0.81$) for specimen I10, and it is at this load that the deviation between analysis and experiment begins to manifest itself in postbuckling on the plot of load versus end shortening in Fig. 4. However, first-ply failure criteria did not indicate failure in the specimen at 18,750 lbs. Transverse matrix cracks, if present, can influence the neighboring interlaminar stress state. For instance, transverse matrix cracks in 90-degree plies can significantly reduced the load for delamination initiation at the straight free edge for tensile/compression coupons (Kim, 1989). Also, Kim (1989) cites difficulties in predicting the onset of delamination when it is primarily driven by interlaminar shear stress τ_{zx} in combination tensile interlaminar normal stress τ_{zz}. The complexity of the stress fields during postbuckling of the flange, and the influence of ply damage on this response, make the prediction of crippling by flange free edge delamination a difficult task.

References

Bonanni, D.L., Johnson, E. R., and Starnes, J.H., Jr., 1991, "Local Crippling of Thin-Walled Graphite-Epoxy Stiffeners," *AIAA Journal*, **29**, 11, November, 1951-1959.

Brewer, J. C., and Lagace, P. A., 1988, "Quadratic Stress Criterion for Initiation of Delamination," *Journal of Composite Materials*, **22**, December, 1141-1155

Davies, G. A. O., Buskell, N., and Stevens, K. A., 1986, "Edge Effects in Failure of Compression Panels," *Mechanical Behaviour of Composites and Laminates*, eds: W. A. Green and M. Micunovic, Eslevier Applied Science, London, 1-11.

Dávila, Carlos G., 1993, "User's Manual for Transition Elements In Processor ES16", The Computational Structural Mechanics Testbed, NASA Langley Research Center, Hampton, VA 23681-0001, February.

Kim, R. Y., 1989, "Experimental observations of free-edge delamination," *Interlaminar Response of Composite Materials*, ed: N. J. Pagano, Elsevier Science Publishers B. V., 111-160.

Kim, R. Y., and Soni, S. R, 1986, "Failure of Composite Laminates due to Combined Interlaminar Normal and Shear Stresses," *Composites '86: Recent Advances in Japan and the United States*, eds K. Kawata, S. Umekawa, and A. Kobayashi, Japan Society for Composite Material, Tokyo, Japan, 341-350.

Rehfield, L. W., and Reddy, A. D., 1986, "Observations on Compressive Local Buckling, Postbuckling and Crippling of Graphite/Epoxy Airframe Structure," Proceedings of the AIAA/ASME/ASCE/AHS 27th Structures, Structural Dynamics and Materials Conference, San Antonio, Texas, May, AIAA Paper No. 86-0923, 310-306.

Starnes, J. H., Jr., and Rouse, M., 1981, "Postbuckling and Failure Characteristic of Selected Flat Rectangular Graphite-Epoxy Plates Loaded in Compression," Proceedings of the AIAA/ASME/ASCE/AHS 22nd Structures, Structural Dynamics and Materials Conference," Atlanta, Georgia, April 6-8, 423-434.

Stewart, C. B., 1989, "The Computational Structural Mechanics Testbed User's Manual," NASA Technical Memorandum 100644, October.

Sun, C. T., and Li, Sijian, 1988, "Three-Dimensional Effective Elastic Constants for Thick Laminates," *Journal of Composite Materials*, **22**, July, 629-639.

Graduate research assistant

Ms. F. Aylin Barlas is the graduate assistant on this project, and this work is the basis for her master's thesis in Aerospace Engineering.

Table 1: Experimental data for I-specimens (Bonanni, et al., 1991)

	Specimen I2	Specimen I10
Average wall thickness t in inches	0.0455	0.0833
Flange width b_f in inches	1.262	1.263
Web height b_w in inches	1.247	1.25
Corner radius r in inches	0.125	0.125
Specimen length L in inches	7.944	5.916

Table 1: Experimental data for I-specimens (Bonanni, et al., 1991)

	Specimen I2	Specimen I10
Gage length l_g in inches	5.944	3.916
Buckling load P_{cr} in pounds	2,786.	16,875.
Crippling load P_{cc} in pounds	10,289.	22,475.
Location of damage initiation	corner	free edge of flange

Table 2: Material property data used in analysis

AS4/3502 Graphite/Epoxy	Specimen I2	Specimen I10
Fiber direction modulus E_{11} in Msi	17.0	17.5
Transverse direction modulus E_{22} in Msi	1.64	
Thickness direction modulus E_{33} in Msi	1.64	
Major Poisson's ratio ν_{12}	0.3	
Minor Poisson's ratio ν_{13}	0.3	
Poisson's ratio ν_{23}	0.35	
Shear moduli G_{12} and G_{13} in Msi	0.87	
Shear modulus G_{23} in Msi	0.49	
Longitudinal interlaminar shear strength Z^{S1} in ksi	13.5	
Transverse interlaminar shear strength Z^{S2} in ksi	13.5	
Tensile (peel) interlaminar strength Z^{T} in ksi	7.54	
Beam-column material for insert at junctions		
Modulus of elasticity in Msi	10.0	13.5

Table 3: Maximum value of the dimensionless delamination index F, the corresponding interlaminar stresses, and the location of this maximum for specimens I2 and I10.

ID	Load P/P_{cc}[a]	F_{max}	Interlaminar stresses for F_{max}; psi			Location along free edge	
			τ_{zz}	τ_{zy}	τ_{zx}	x in inches[b]	Interface[c]
I2	1.03	0.247	2,674.	-2,322.	-4,094.	4.06 (NP)	0/90 (3)
	0.92	0.008	-893.	-42.	839.	5.48 (BC)	45/0 (2)
	1.02	0.400	-515.5	1,212.	8,642.	6.24 (IP)	90/0 (4)
I10	1.03	0.02	-1,609.	1,389	-1,386.	2.80 (BC)	0/90 (3)
	1.03	0.73	-1,961.	1,438.	-11,423.	2.03 (IP)	0/90 (3)

a. P_{cc} is the crippling load listed in Table 1.
b. Letters in parentheses refer to deflection pattern on free edge: NP⇒near node point; BC⇒near buckle crest; IP⇒near inflection point.
c. The number in parentheses corresponds to the interface numbers shown in Fig. 5.

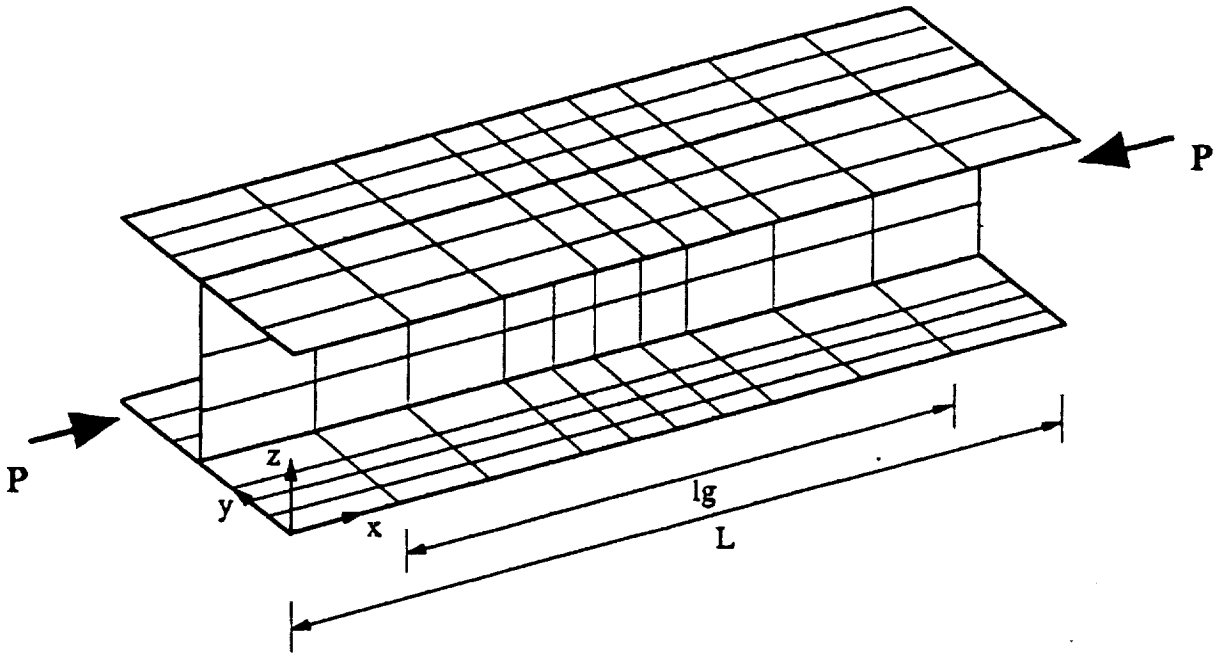

Fig. 1 The branched-shell finite element model of an I-section stiffener.

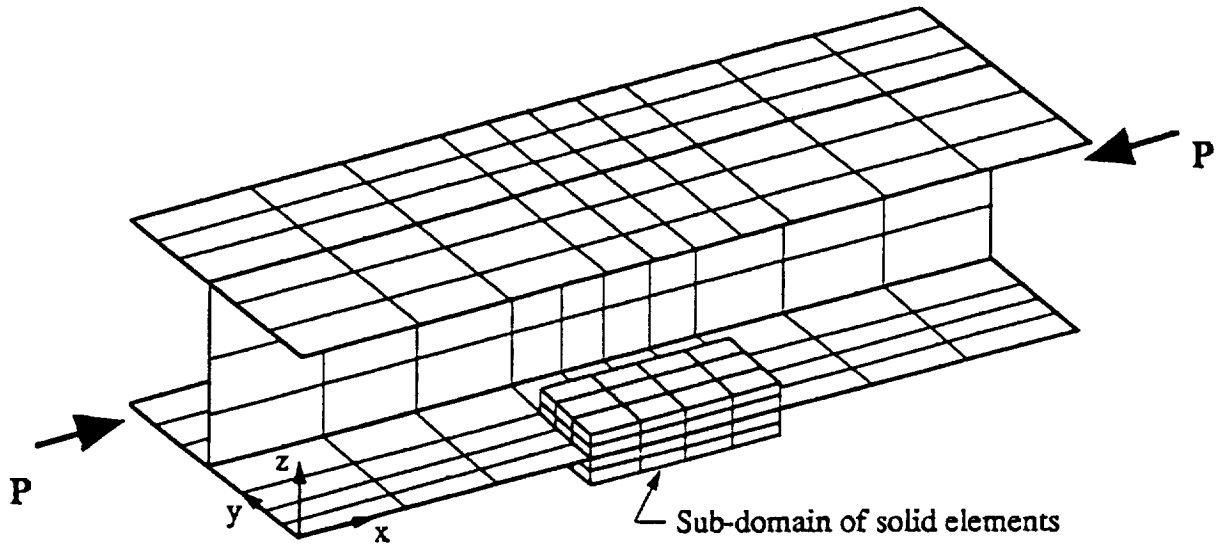

Fig. 2 The complex model of the I-section stiffener showing a sub-domain containing transition and solid elements at the free edge of a flange.

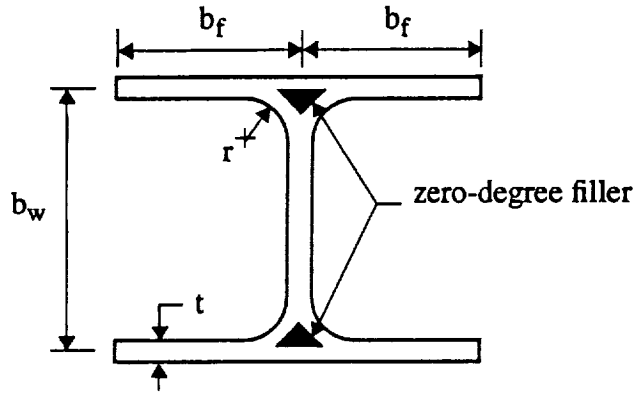

Fig. 3 Cross section of an I-section stiffener that is fabricated from graphite-epoxy unidirectional tape. Unidirectional filler material is required during layup to fill the void at the junctions of the flanges and web.

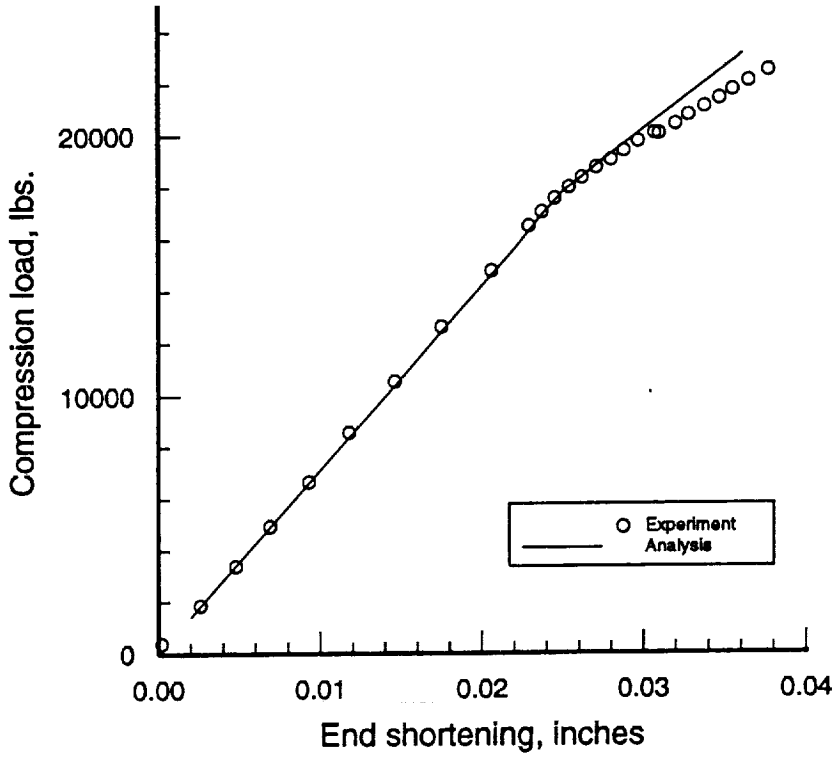

Fig. 4 Comparison of the branched shell analysis and experiment for specimen I10 on the load-end shortening plot.

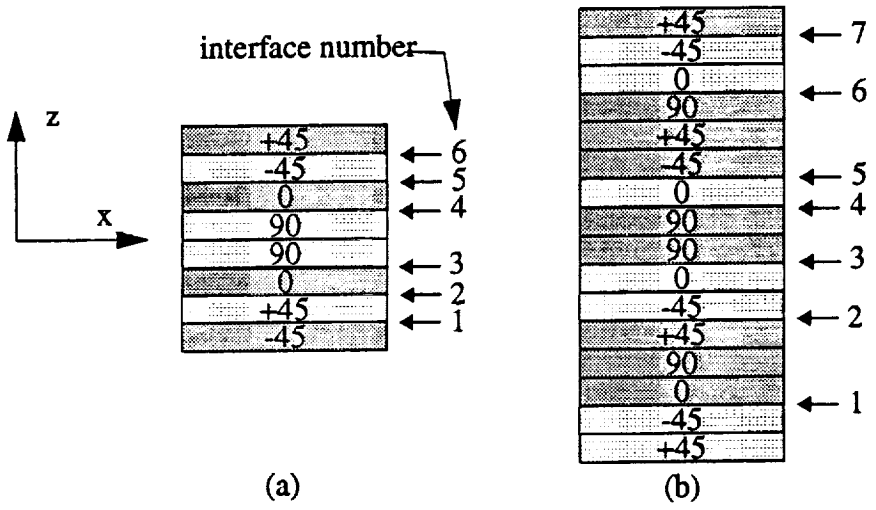

Fig. 5 Distribution of BR20 brick elements through the thickness of a flange. (a) Seven elements and six interfaces for specimen I2. (b) Eight elements and seven interfaces for specimen I10.

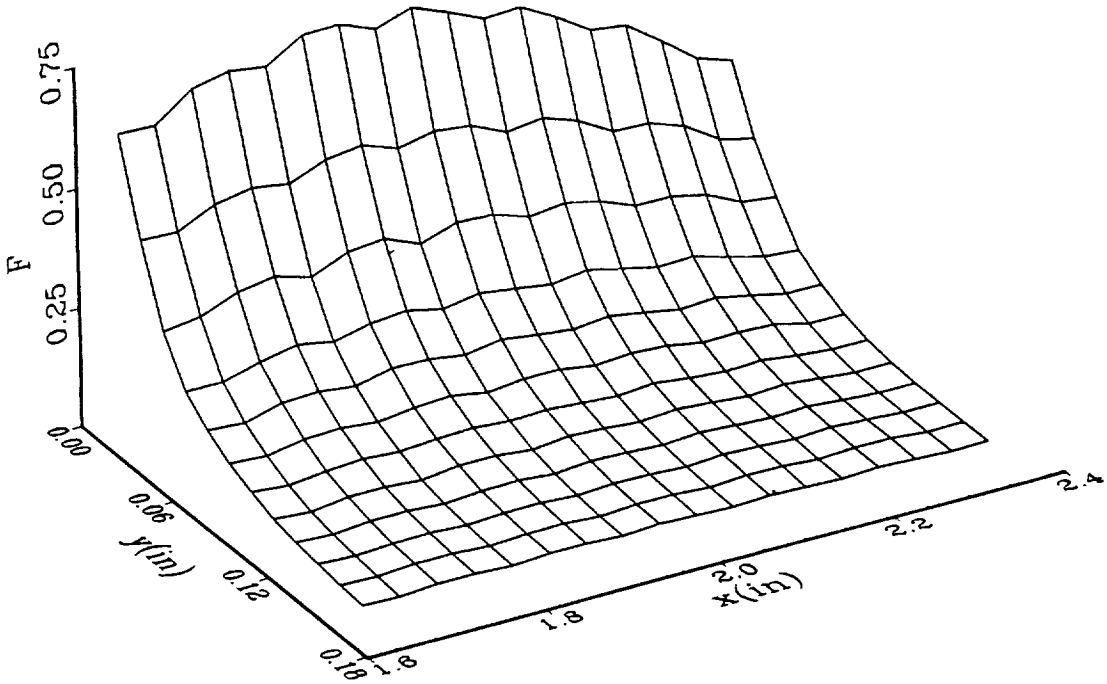

Fig. 6 Distribution of the dimensionless delamination index *F* in a 0/90 interface for specimen I10 at P/P_{cc} =1.03. This is interface 3 in Fig. 5(b). The free edge of the flange is at y = 0.

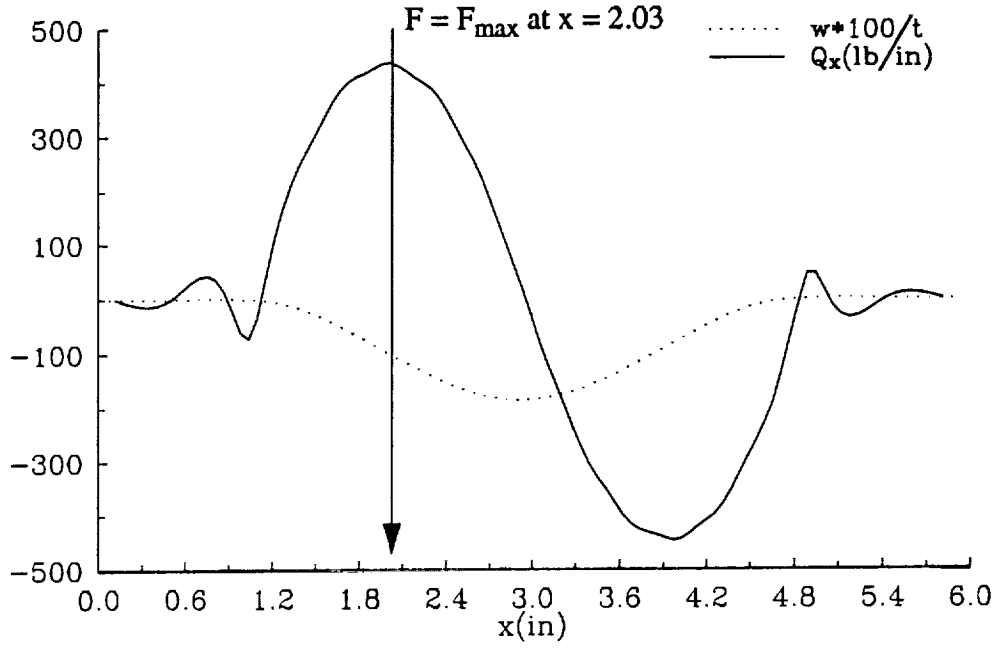

Fig.7 The distribution of the out-of-plane displacement normalized by the flange thickness and the transverse shear resultant Q_x along the free edge of the flange for specimen I10 from the branched shell model.

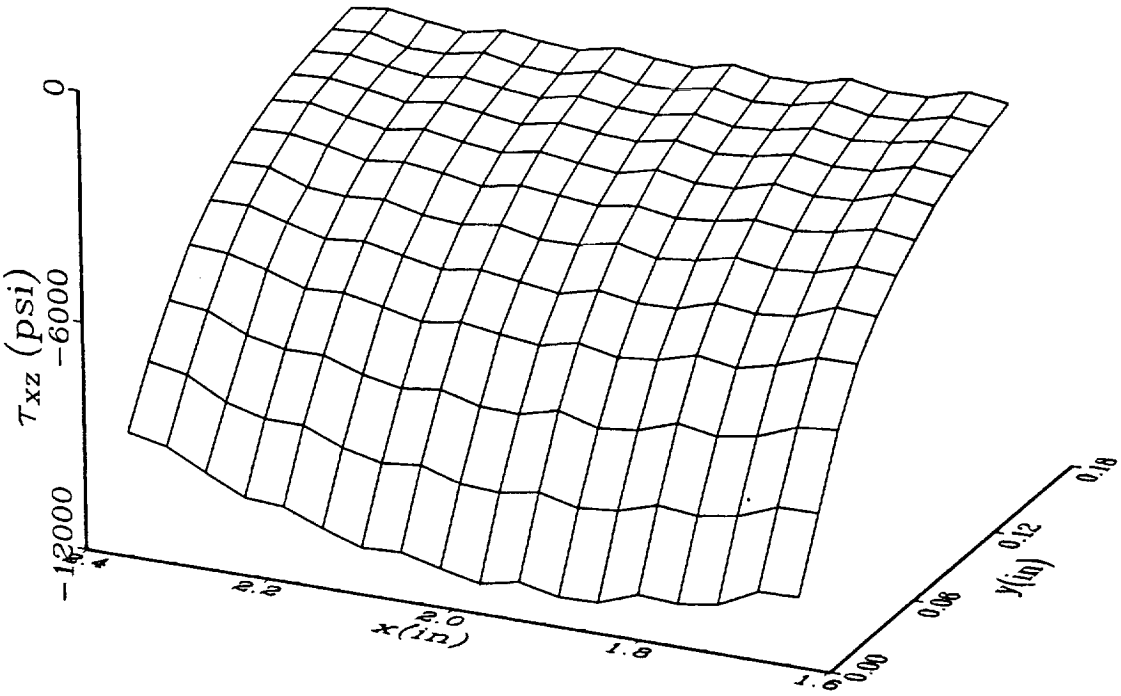

Fig.8 Distribution of the interlaminar shear stress component tangent to the free edge the 0/90 interface of specimen I10 at P = 1.03 P_{cc}.

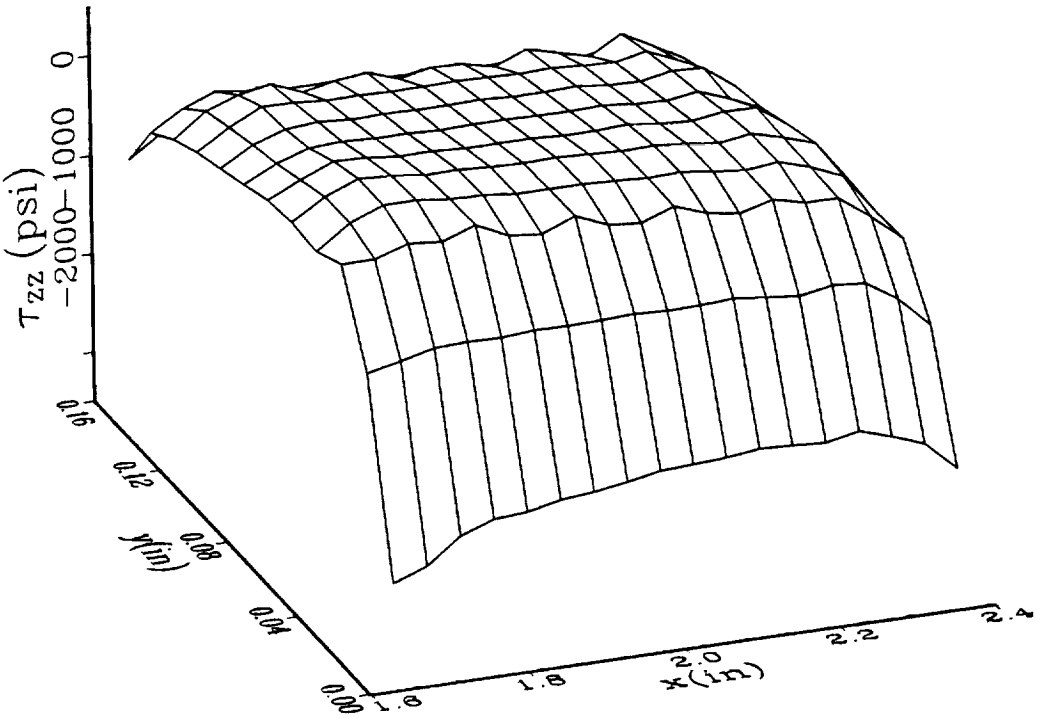

Fig.9 Distribution of the interlaminar normal stress component in the 0/90 interface o specimen I10 at P = 1.03 P_{cc}.

II. Pressure Pillowing of an Orthogonally Stiffened Cylindrical Shell

Background and objectives

The cabin pressure in a transport aircraft causes about a 10 psi pressure differential across the skin. An unstiffened, or monocoque, fuselage would carry this internal pressure load as a shell in membrane response, like a pressure vessel. However, internal longitudinal and transverse stiffeners are necessary to carry maneuver loads, etc. The presence of these internal stiffeners prevents the fuselage skin from expanding as a membrane, and the skin bulges, or "pillows", between the stiffeners under the action of the internal pressure. Where the skin is restrained against its expansion as a membrane along the stiffeners, a bending boundary layer is formed. Also, at the stiffener intersection a local concentration of the interacting loads between the stiffeners and the skin occurs.

The objectives of this project are 1) to analyze the concentration of the interacting loads at the stiffener intersection, and 2) to study the pillowing of the skin.

Photocopies of the transparencies used for the presentation at the *34th SDM* conference appear in the Appendix of this report. These transparencies are the basis of much of the following discussion, and the page numbers referred to in the text refer to the page numbers labeled on the transparencies.

Mathematical model

An idealized mathematical model is assumed for the semi-monocoque fuselage to study the generic characteristics of the response in the vicinity of the stiffener intersection. The model is of a very long circular cylindrical shell internally stiffened by identical stringers equally spaced around the circumference, and identical frames, or rings, equally spaced along the length as shown on page 2. In general, the spacing of the stringers is not the same as the rings. The structure is periodic both longitudinally and circumferentially, and the loading is spatially uniform. Consequently, a structural repeating unit can be defined whose deformation determines the deformation of the entire structure. The repeating unit consists of a portion of the shell wall centered over portions of the stringer and ring as shown page 3. The radius of the middle surface of the undeformed cylinder is denoted by R, stringer spacing by b, and frame spacing is denoted by L. Axial and circumferential arc length coordinates are denoted by x and y, respectively.

The stiffeners are modeled as mathematically one-dimensional structural elements, such that the actions transmitted by the stiffeners to the inside surface of the shell wall are represented by distributed line loads as shown on page 4. Coordinate ξ is an axial coordinate whose origin is centered over the stiffener intersection, θ is the circumferential angle, and ζ is the normal coordinate to the shell reference surface. It is assumed that the stringer is symmetric about the ξ-ζ plane through its centroidal axis, and the ring is symmetric about the θ–ζ plane through its circular reference axis. On the basis of the symmetry about the ξ– and θ– axes for the unit, only the interacting load components tangent and normal to the stiffeners are included in the analysis. The interacting load intensities per unit undeformed length along the contact lines are denoted by $\lambda_{x1}(\xi)$ for the component tangent to the stringer, $\lambda_{\zeta 1}(\xi)$ for the component normal to the stringer, $\lambda_{y2}(\theta)$ for the component tangent to the ring, and by $\lambda_{\zeta 2}(\theta)$ for the component normal to the ring.

The positive directions for these interacting loads acting on the shell are shown on page 4. The purpose of the analysis is to determine these distributed line loads.

An enclosed volume to contain the pressurized medium is modeled by assuming diaphragms to extend from the edges of the repeating unit to the axis of revolution of the cylinder. The diaphragms do not resist the deformation of the repeating unit, but act to transmit loads normal to the edges of the repeating unit due to the internal pressure.

For the linear elastic response of the repeating unit to internal pressure, we use the Ritz method and the principle of virtual work augmented by Lagrange multipliers to enforce kinematic constraints between the structural components of the repeating unit. See page 5. The Lagrange multipliers represent the interacting line loads between the stiffeners and the shell. Displacements are separately assumed for the shell, stringer, and ring. The shell is modeled with Sander's theory or the Donnell-Mushtari-Vlasov (DMV) quasi-shallow shell theory.

Displacement and Lagrange multiplier approximations

The periodic portions of the displacements are represented by truncated Fourier Series, and the nonperiodic portions of the displacements due to axial stretching are represented by simple terms in ξ. For the shell, the displacements of the middle surface are

$$u(\xi, \theta) = \sum_{m=1}^{M} \sum_{n=0}^{N} u_{mn} \sin(\alpha_m \xi) \cos(\beta_n \theta) + \frac{q_0 \xi}{2l}, \tag{2}$$

$$v(\xi, \theta) = \sum_{m=0}^{M} \sum_{n=1}^{N} v_{mn} \cos(\alpha_m \xi) \sin(\beta_n \theta), \tag{3}$$

$$w(\xi, \theta) = \sum_{m=0}^{M} \sum_{n=0}^{N} w_{mn} \cos(\alpha_m \xi) \cos(\beta_n \theta), \tag{4}$$

in which $\alpha_m = (m\pi)/l$ and $\beta_n = (n\pi)/\Theta$ where m and n are non-negative integers, and $l = L/2$. The displacements of the centroidal axis of the stringer are

$$u_s(\xi) = \sum_{m=i}^{M} u_{sm} \sin(\alpha_m \xi) + \frac{q_1 \xi}{2l} \qquad w_s(\xi) = \sum_{m=0}^{M} w_{sm} \cos(\alpha_m \xi) \tag{5}$$

Parameters q_0 in the axial displacement of the shell and q_1 in the axial displacement of the stringer represent elongations of each respective element caused by either an axial mechanical load or due to closed-end pressure vessel effects. The displacements of the reference circle of the ring are

$$v_r(\theta) = \sum_{n=1}^{N} v_{rn} \sin(\beta_n \theta) \qquad w_r(\theta) = \sum_{n=0}^{N} w_{rn} \cos(\beta_n \theta) \tag{6}$$

The distributions of the Lagrange multipliers, or interacting loads, are taken as

$$\lambda_{x1} = \sum_{m=1}^{M} \lambda_{x1m} \sin(\alpha_m \xi) \qquad \lambda_{\zeta 1} = \sum_{m=1}^{M} \lambda_{\zeta 1m} \cos(\alpha_m \xi), \tag{7}$$

$$\lambda_{y2} = \sum_{n=1}^{N} \lambda_{y2n} \sin(\beta_n \theta) \qquad \lambda_{\zeta 2} = \sum_{n=0}^{N} \lambda_{\zeta rn} \cos(\beta_n \theta). \tag{8}$$

Note that in the stringer interacting normal load, the term $\lambda_{\zeta 1,0}$, which represents a uniformly distributed load, is omitted. Since the stringer as modeled by this analysis is not restrained from rigid body motion in the radial direction the resultant normal load on the stringer must vanish; i.e.,

$$\int_{-l}^{l} \lambda_{\zeta 1}(\xi)\, d\xi = 0, \tag{9}$$

and this condition requires $\lambda_{\zeta 1,0}$ to vanish.

Discrete equations and their solution

The discrete displacement vector for the shell is the $(3MN+2M+2N+2) \times 1$ vector

$$\hat{u}_{shell} = [\hat{u}_0^T, \hat{u}_1^T, \ldots, \hat{u}_M^T]^T \tag{10}$$

in which the subvectors are

$$\begin{aligned} \hat{u}_0 &= [q_0, w_{00}, v_{01}, w_{01}, \ldots, v_{0N}, w_{0N}]^T \\ \hat{u}_m &= [u_{m0}, w_{m0}, u_{m1}, v_{m1}, w_{m1}, \ldots u_{mN}, v_{mN}, w_{mN}]^T \qquad m = 1, \ldots, M \end{aligned} \tag{11}$$

The $(2M + 1) \times 1$ discrete displacement vector for the stringer and the $(2N + 1) \times 1$ vector for the ring are

$$\hat{u}_{str} = [q_1, u_{s1}, w_{s1}, \ldots, u_{sM}, w_{sM}]^T \qquad \hat{u}_r = [w_{r0}, v_{r1}, w_{r1}, \ldots, v_{rN}, w_{rN}]^T, \tag{12}$$

in which the term w_{s0} for the stringer has been omitted since it does not deform the stringer and its conjugate resultant satisfying Eq. (9) is equal to zero. This uniform normal displacement component is determined from the condition that the rigid body displacement of the stringer is the uniform portion of the normal displacement component of the shell at $\theta = 0$; i.e.,

$$\sum_{n=0}^{N} w_{0n} = w_{s0}. \tag{13}$$

The discrete vectors of the Lagrange multipliers for the stringer and ring, are

$$\lambda_1 = [\lambda_{x11}, \lambda_{\zeta 11}, \ldots, \lambda_{x1M}, \lambda_{\zeta 1M}] \qquad \lambda_2 = [\lambda_{\zeta 20}, \lambda_{y21}, \lambda_{\zeta 21}, \ldots \lambda_{y2N}, \lambda_{\zeta 2N}]\,, \tag{14}$$

respectively.

A schematic of the Lagrange multipliers and the conjugate displacements along the contact line between the shell and stringer is shown on page 6. These variables constitute the terms in the external virtual work for the shell and stringer. Similar terms are used for the external virtual work to represent the contact between the shell and ring. The pressure is treated as a dead load in the linear analysis, and contributes to the external virtual work for the shell. The applied axial load P is shared between the shell and stringer. To account for load sharing, a Lagrange multiplier Q is used to denote that portion of the axial load P carried by the stringer. Thus, P - Q is carried by the shell. In the results that are presented below axial load P is prescribed to equal the closed-end pressure vessel force that is carried by one repeating unit.

The discrete system of equations for the linear response of the repeating unit are shown on page 7. The first three rows represent equilibrium equations for the shell, stringer, and ring, respectively. The fourth row represents the kinematic constraints between the shell and stringer, fifth row represents the kinematic constraint between the shell and ring, and sixth row represents the fact that the net elongation of the shell and stringer are equal. The right-hand side vector contains terms determined by the internal pressure. The size of this system for M = N = 24 is shown in the table on page 8.

Numerical example

Data for the example shown on page 9 are taken from an example solved by Wang and Hsu (1985), and the dimensional data is representative of a large transport fuselage. The shell wall stiffness matrices given by

$$A = \begin{bmatrix} 0.664 & 0.221 & 0 \\ 0.221 & 0.577 & 0 \\ 0 & 0 & 0.221 \end{bmatrix} \times 10^6 \text{ lb/in} \qquad B = 0 \qquad D = \begin{bmatrix} 262 & 159 & 4.33 \\ 159 & 210 & 4.33 \\ 4.33 & 4.33 & 159 \end{bmatrix} \text{ lb-in}\,,$$

in which A denotes the membrane stiffness matrix, B the coupling matrix, and D denotes the bending stiffness matrix of classical lamination theory.

All the results presented for this example are for an internal pressure p = 10 psi. The Fourier Series were truncated at $M = N = 24$. Since $b/R = 2.83°$, the shell in this example is shallow and the DMV (Donnell-Mushtari-Vlasov) shell theory should be adequate. We found that the numerical results using Sanders theory with the rotation about the normal neglected and the numerical results using DMV theory were essentially the same.

Results

The axial distributions of the shell normal displacement w at three circumferential positions is shown on page 11. These displacements for the stiffened shell are all lower than the normal displacement of 0.229 in. for the membrane shell (no stiffeners). The largest normal displacement of the shell occurs midway between the stiffeners, and its minimum occurs at the stiffener intersection. The difference in these displacements is a measure of pillowing. Comparison of these results to those of Wang and Hsu (1985) (their Fig. 5) show excellent agreement.

The axial normal strain distributions on the outside surface and inside surface of the shell are shown on page 12. For the data plotted along $y = 0$, a large bending strain (difference in the surface strains) gradient is evident as the ring is approached. This axial bending strain gradient at the ring midway between the stringers is also a result of panel pillowing. The outside and inside surface axial strain distributions along the circumference at $x = 0$ are equal (no bending), and are nearly uniform, decreasing slightly as the stringer is approached. Wang and Hsu (1985) show a larger decrease in the axial strain as the stringer is approached along the circumferential direction midway between the rings (see their Fig. 6). Otherwise, the results shown on page 12 compare very well to those presented by Wang and Hsu.

The interacting normal load intensity acting on the shell due to the contact with the stringer is shown on page 13. A positive value means the stringer is forcing the shell radially outward. Since the integral of this distribution is zero, the area under this curve is zero. The large spike at the stiffener intersection is counteracted by small negative mean value over the region outside the intersection. The Fourier Series results for this load suggests a singularity, or non convergence, at the stiffener intersection. It was found that for an increasing number of harmonics in the truncated series, the peak value at the intersection increased and frequency of the oscillations about the negative mean value increased. Wang and Hsu (1985) do not present results for the interacting loads.

The interacting normal load intensity acting on the shell due to the contact with the ring is shown on page 14. A very large negative peak value occurs at the stiffener intersection indicating the ring is pulling the shell radially inward. Again this distribution suggests the Fourier Series is attempting to model a singularity at the stiffener intersection.

Peak values of the interacting normal loads acting on the shell at the stiffener intersection are plotted versus an increasing number of harmonics ($M = N$) on page 15. Note that the algebraic sum of the two loads is negative, meaning combined effect of both stiffeners is to pull the shell radially inward against the internal pressure force. These peak load intensities increase monotonically as the number of harmonics increase. Thus, no convergence is apparent in the range of M and N shown in the plot.

The concluding remarks on are given on page 16. The interacting normal load intensities exhibit singular behavior at the stiffener intersection, or the stiffener crossing point. Results compare well to Wang and Hsu's (1985) results, except for the axial strain decrease in the θ-direction at the stringer midway between the rings.

Investigations of the axial strain distribution in the shell near the stringer

We tried several methods to investigate if the axial strain decreases in the θ-direction as the stringer is approached. First additional terms were added to the displacement expansions, second a finite element solution in the axial direction and Fourier Series in the circumferential direction was tried, third an analytic method for a cylindrical shell stiffened by stringers only was tried, and fourth Wang and Hsu's (1985) equations were programmed directly.

Additional displacement terms: The following terms were added to Eqs. (2-4)

$$u_p = \frac{\xi}{2l}\sum q_n \cos(\beta_n \theta) \qquad v_p = \frac{\xi^2}{2lR}\sum l_n \sin(\beta_n \theta) \qquad w_p = \frac{\xi^2}{4lR}\sum s_n \cos(\beta_n \theta) \qquad (1)$$

in which q_n, l_n, and s_n are additional discrete degrees of freedom. The rationale for these additional terms is as follows: A term like $\xi\, q_1 \cos(\beta_1\, \theta)$ in the axial displacement permits a circum-

ferential variation in the axial strain that is independent of ξ. Quadratic terms in ξ in the v-displacement expansion and the w-displacement expansion are consistent with symmetry about the ring, and pemit zero addtional circumferential strain and zero additional in-plane shear strain for particular choices of l_n and s_n. However, the results with these additional terms showed that there were large in-plane shear resultants at $\xi = \pm l$ that did not exist previously. This shear was antisymmetrically distributed about the stringer, and zero at $\theta = \pm \Theta$. The stringer axial load was substantially different than the solution without the additional terms shown above. Thus, this approach was abandoned.

Finite element approximation in the x-direction: Starting with the Fourier Series expansions of the displacements in the circumferential direction, we approximated the fourier series coefficients, or generalized coordinates, with finite element interpolations in the axial coordinate. We had difficulty in selecting the interpolation functions for the Lagrange multipiers, and could not get meaningful results. Thus, we stopped with this approach.

Analytic solution for stringer-stiffened shell only: We found shell resultants that were independent of axial coordinate ξ and satisfied equilibrium. Compatibility equations were solved to get the displacements. Matching the displacements and force conditions with the stringer resulted in a solutions which led us back to spatially uniform resultants and strains. That is, no axial strain reduction in the circumferenitial direction near the stringer was obtained.

Programming of Wang and Hsu's equations: Finally, we programmed the solution given by Wang and Hsu's paper directly. The result from our coding was that there was no reduction in the axial normal strain in the shell as the stringer was approached in the θ-direction. (In Wang and Hsu's paper we calculated coefficients $D_{mn}{}^{u}$ in Eq. (79) and $D_n{}^{u}$ in Eq. (91) to be zero. Non zero values for these coefficients would have given a reduction in the axial strain.)

Graduate research assistant

Naveen Rastogi is the graduate assistant on this project, and this work is the basis of his dissertation for the Doctor of Philosophy degree in Aerospace Engineering.

Interacting Loads in an Orthogonally Stiffened Composite Cylindrical Shell

Eric R. Johnson[1] and Naveen Rastogi[2]

Department of Aerospace and Ocean Engineering
Virginia Polytechnic Institute and State University
Blacksburg, Virginia 24061-0203

Presented in Session 25—Work-in-Progress 1
34th AIAA/ASME/ASCE/AHS/ASC
Structures, Structural Dynamics and Materials Conference
April 19-21, 1993, Hyatt Regency, La Jolla California

Sponsored by NASA Grant NAG-1-537
Dr. James H. Starnes, Jr., Technical Monitor

---

1. Associate Professor; Senior member AIAA; Member ASME
2. Graduate Research Assistant; Student member AIAA

Long circular cylinder internally stiffened by a regular arrangement of frames and stringers

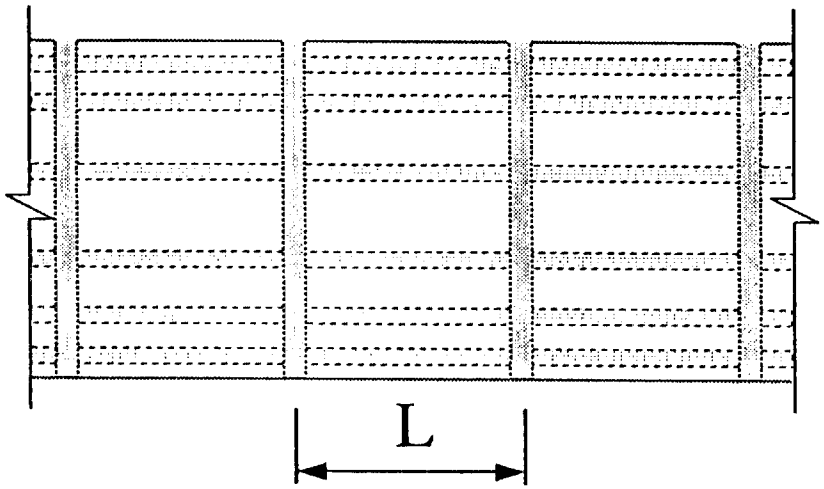

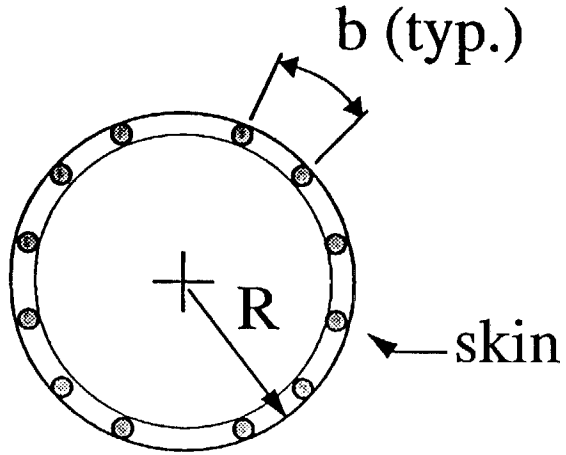

L = frame spacing; b = stringer spacing; R = cylinder radius

- uniform internal pressure p
- axial load P

Repeating structural unit

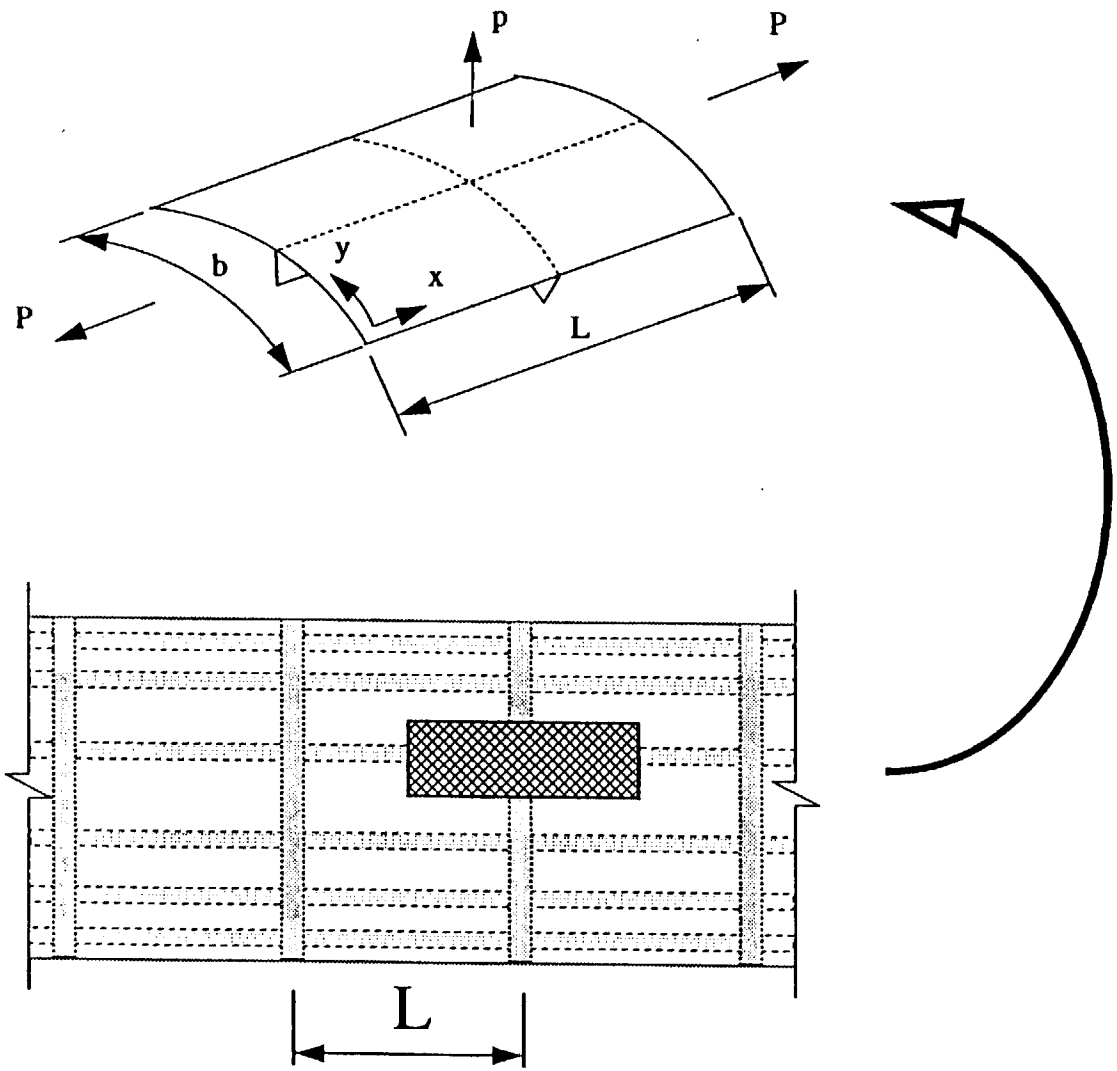

Purpose

To determine the distribution of the interacting loads between the shell and stiffeners

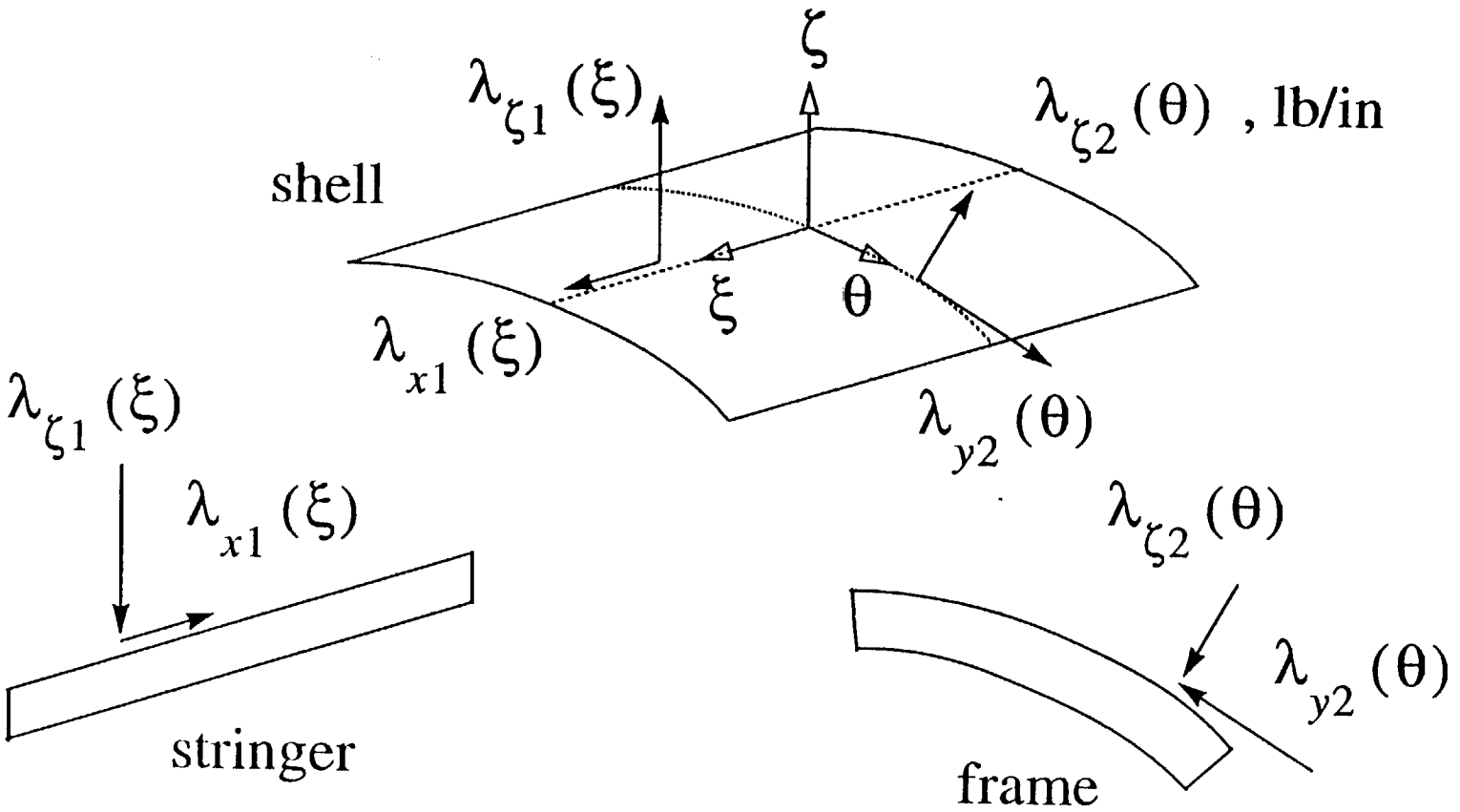

Ritz analysis using augmented virtual work functional

- Assumed displacements distributions for shell, stringer, and ring.
  - periodic part (Fourier Series)
  - particular part (polynomials to account for axial stretching)
- Augment external virtual work with the interacting loads, or Lagrange multipliers.
- Principle of virtual work for each component to get equilibrium equations.
- Displacement constraint equations
  - shell and stringer
  - shell and ring

External virtual work: shell and stringer

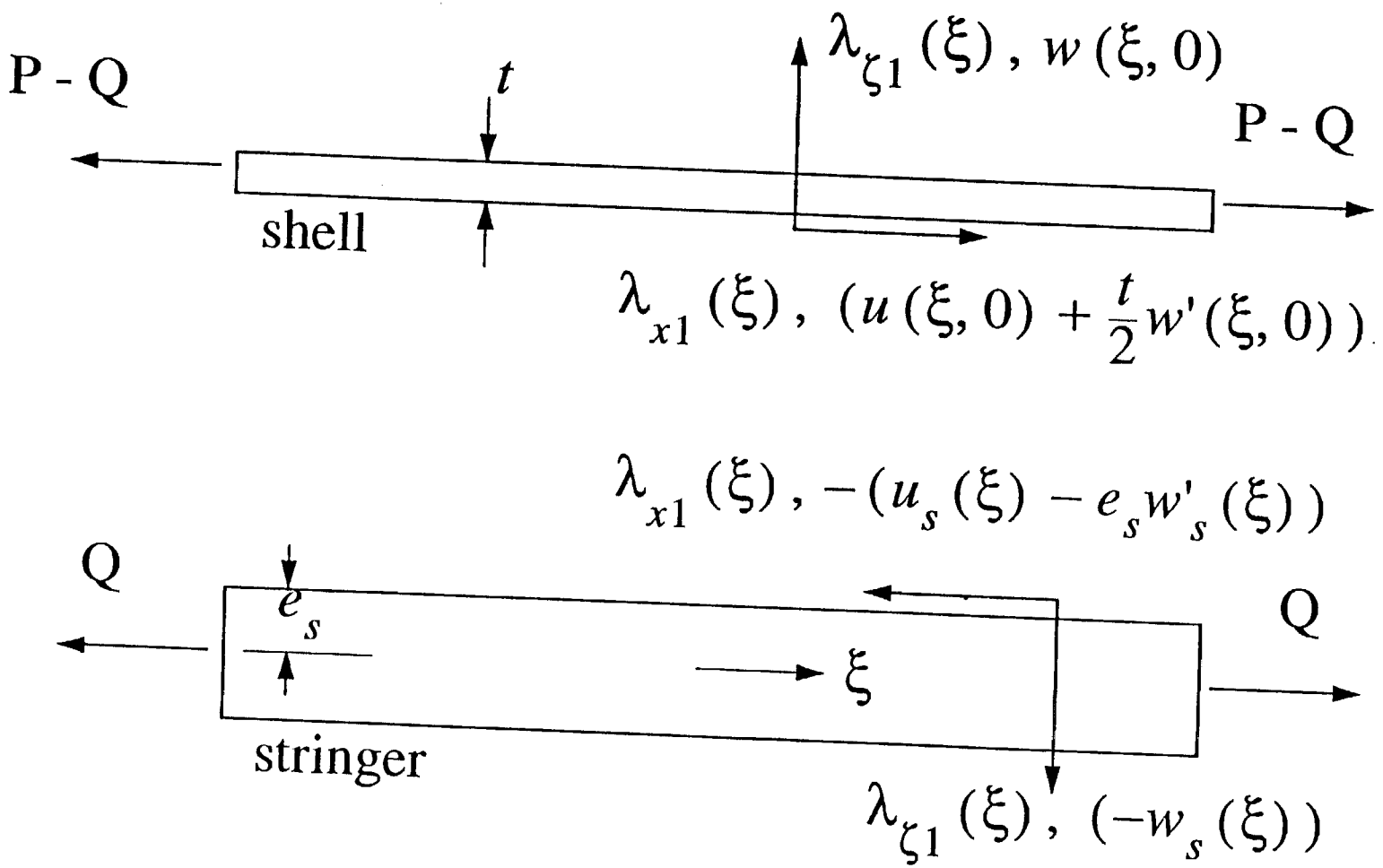

System of Equations

$$\begin{bmatrix} K_{11} & 0 & 0 & B_{11} & B_{12} & B_{13} \\ 0 & K_{22} & 0 & B_{21} & 0 & B_{23} \\ 0 & 0 & K_{33} & 0 & B_{32} & 0 \\ B_{11}^T & B_{21}^T & 0 & 0 & 0 & 0 \\ B_{12}^T & 0 & B_{32}^T & 0 & 0 & 0 \\ B_{13}^T & B_{23}^T & 0 & 0 & 0 & 0 \end{bmatrix} \begin{bmatrix} u_{shell} \\ u_{str} \\ u_r \\ \lambda_1 \\ \lambda_2 \\ Q \end{bmatrix} = \begin{bmatrix} F_{shell} \\ 0 \\ 0 \\ 0 \\ 0 \\ 0 \end{bmatrix}$$

System of Equations for M = N = 24

Sub-vector	DOF's
u_{shell}	1,826
u_{str}	49
u_r	49
λ_1	49
λ_2	49
Q	1
TOTAL	2,022

Numerical Example

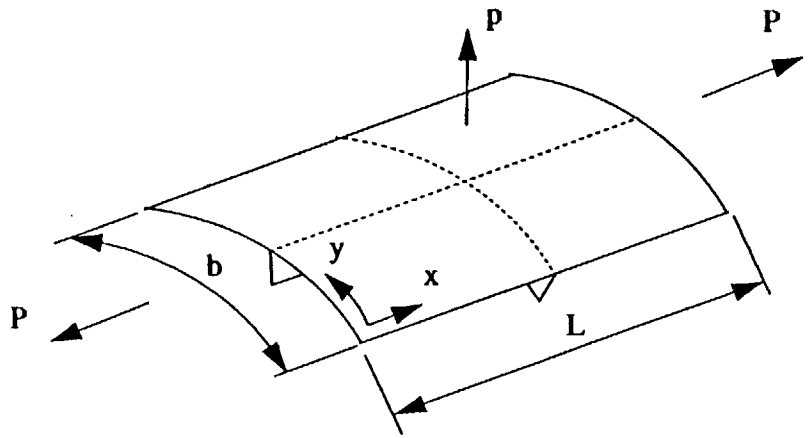

Shell: L = 20 in., R = 117.5 in., b = 5.8 in., t = 0.075in.

Frame: $EI_r = 0.269\times10^8$ lb-in^2 $EA_r = 0.592\times10^7$ lb
$R_0 = 113.72$, and $e_r = 3.78$in.

Stringer: $EI_s = 0.142\times10^8$ lb-in^2 $EA_s = 0.404\times10^7$ lb and
$e_s = 1.10$ in.

Numerical example

Loads: internal pressure p = 10 psi; axial force is due to closed-end pressure vessel effect (P = 3407.5 lb.)

Number of harmonics: M = N = 24 for all the the results which follow.

This problem was originally solved by

- Wang, J. T-S, and Hsu, T-M, "Discrete Analysis of Stiffened Composite Cylindrical Shells," *AIAA Journal*, Vol. 23, No. 11, 1985, pp. 1753-1761.

Wang and Hsu include the interacting loads but do not present results for them.

Axial distributions of the out-of-plane displacement of the shell at three circumferential positions

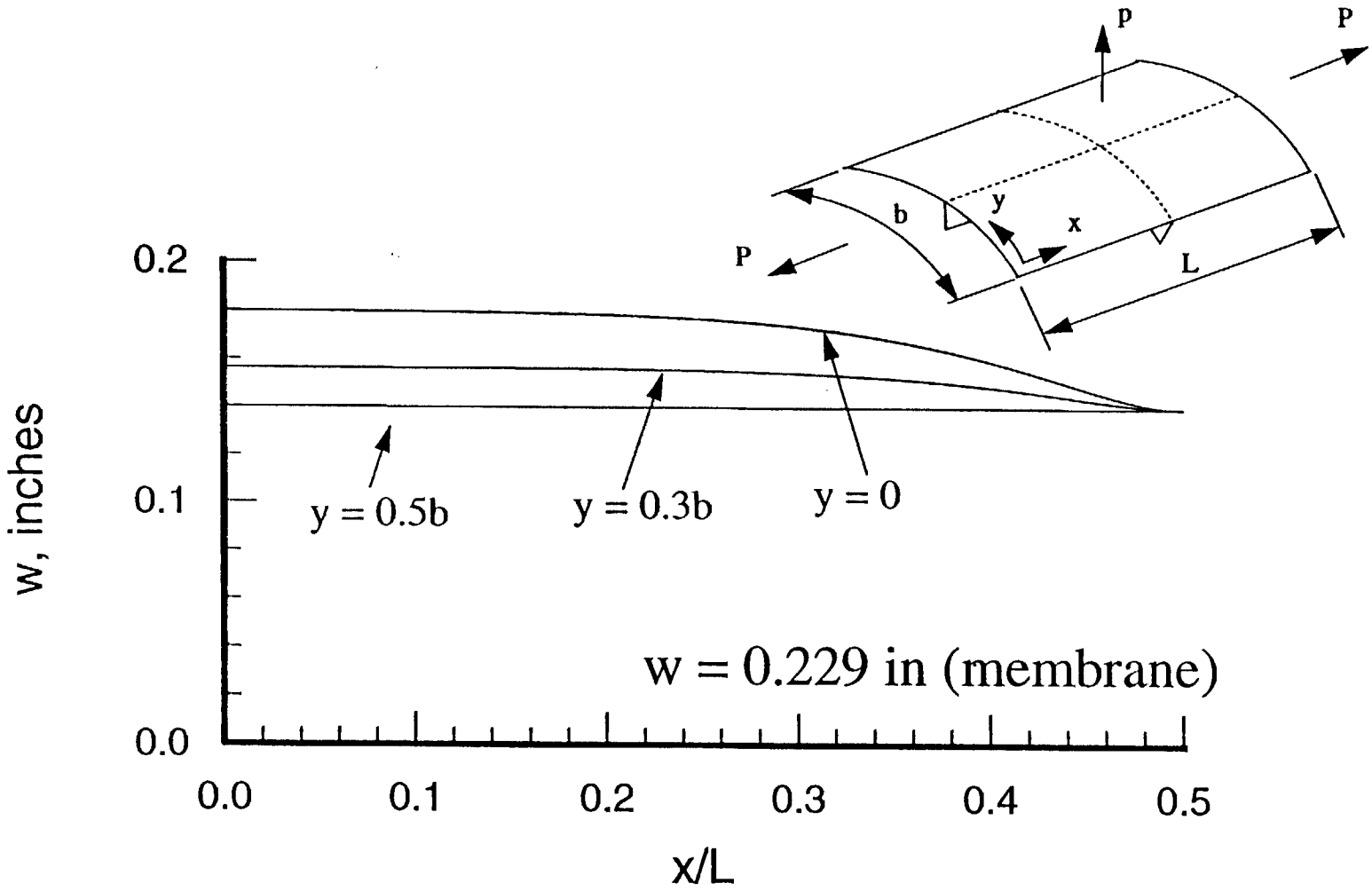

Axial normal strain on shell surfaces

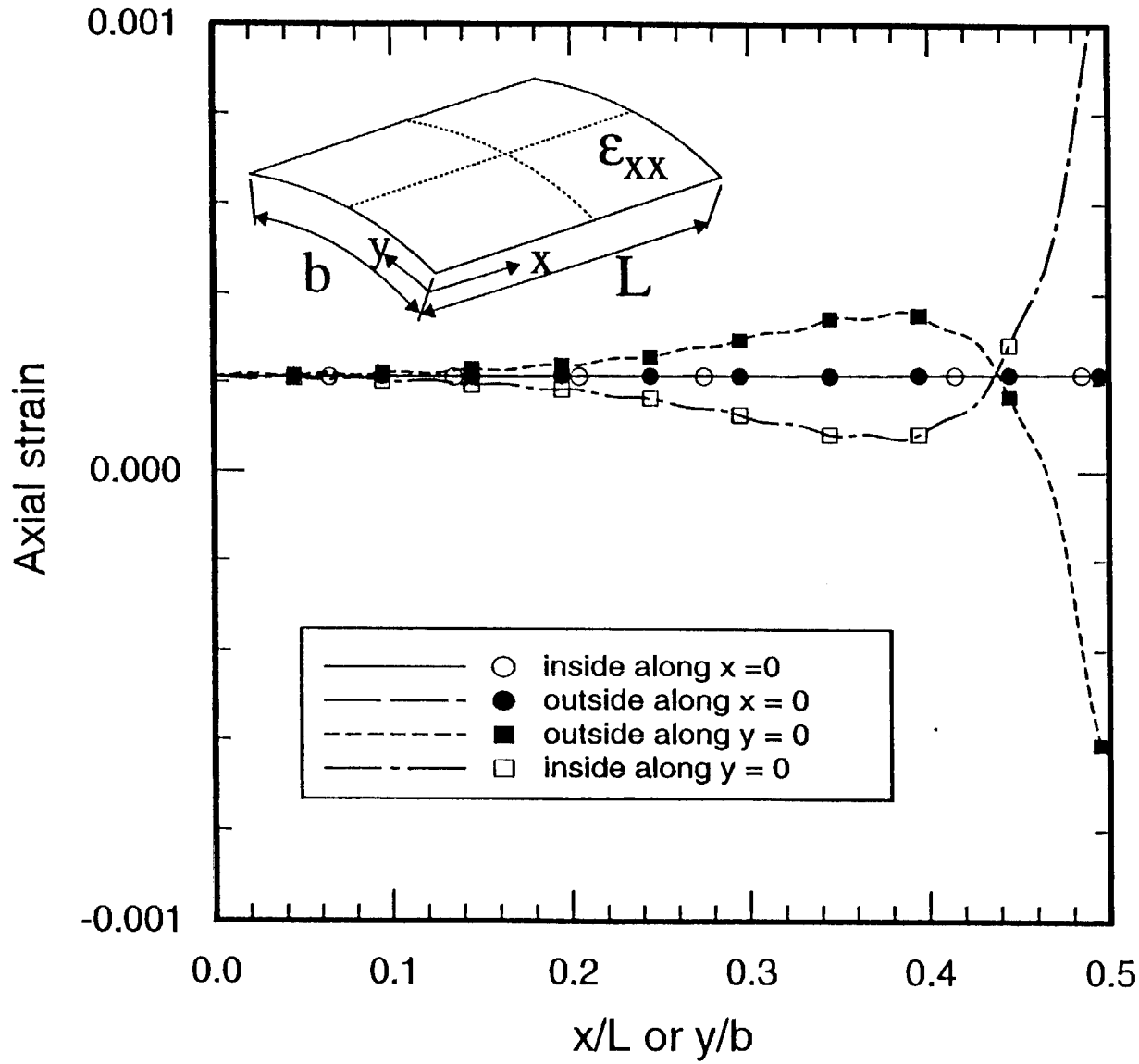

Interacting normal load between shell and stringer

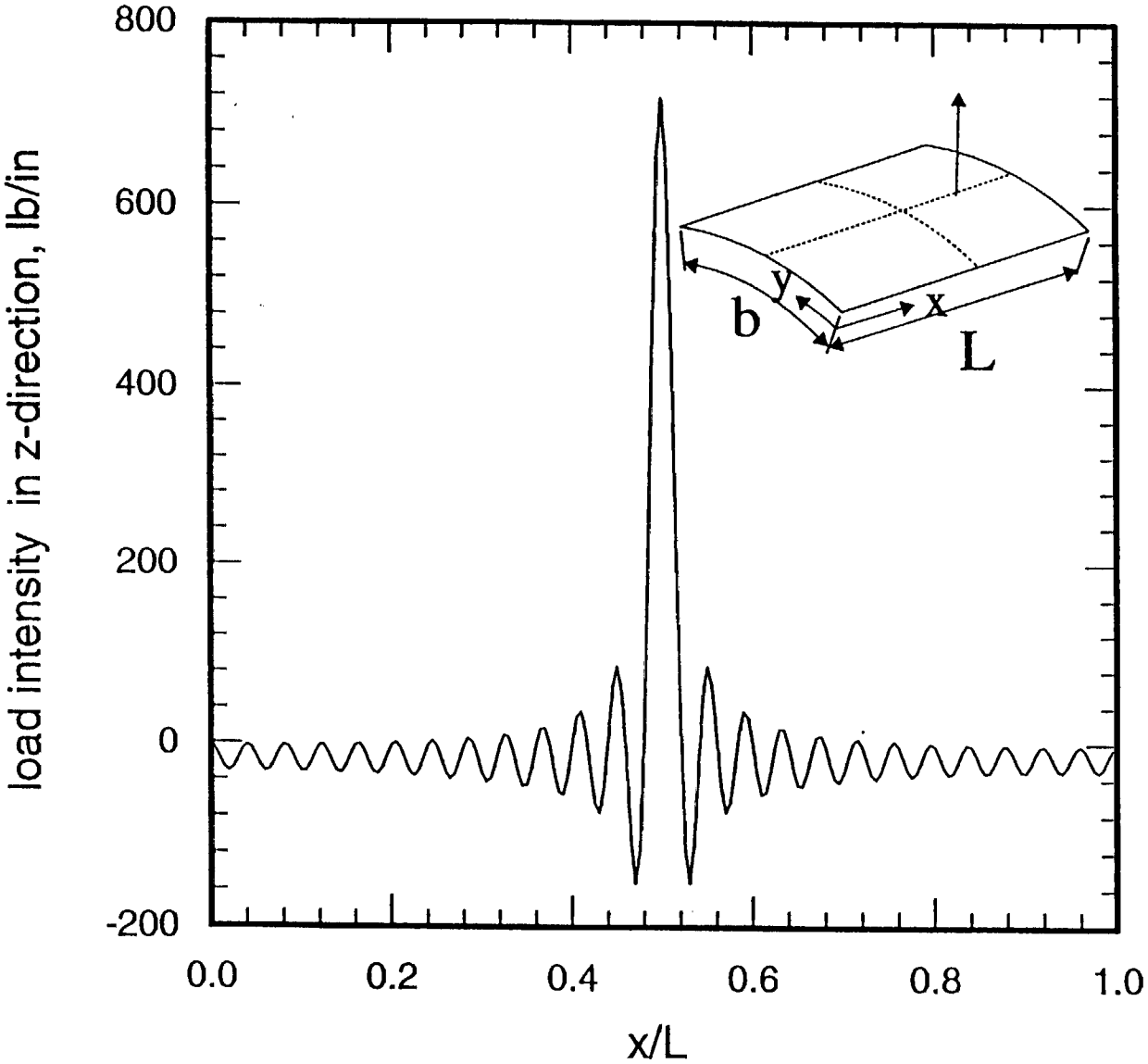

Interacting normal load between shell and frame

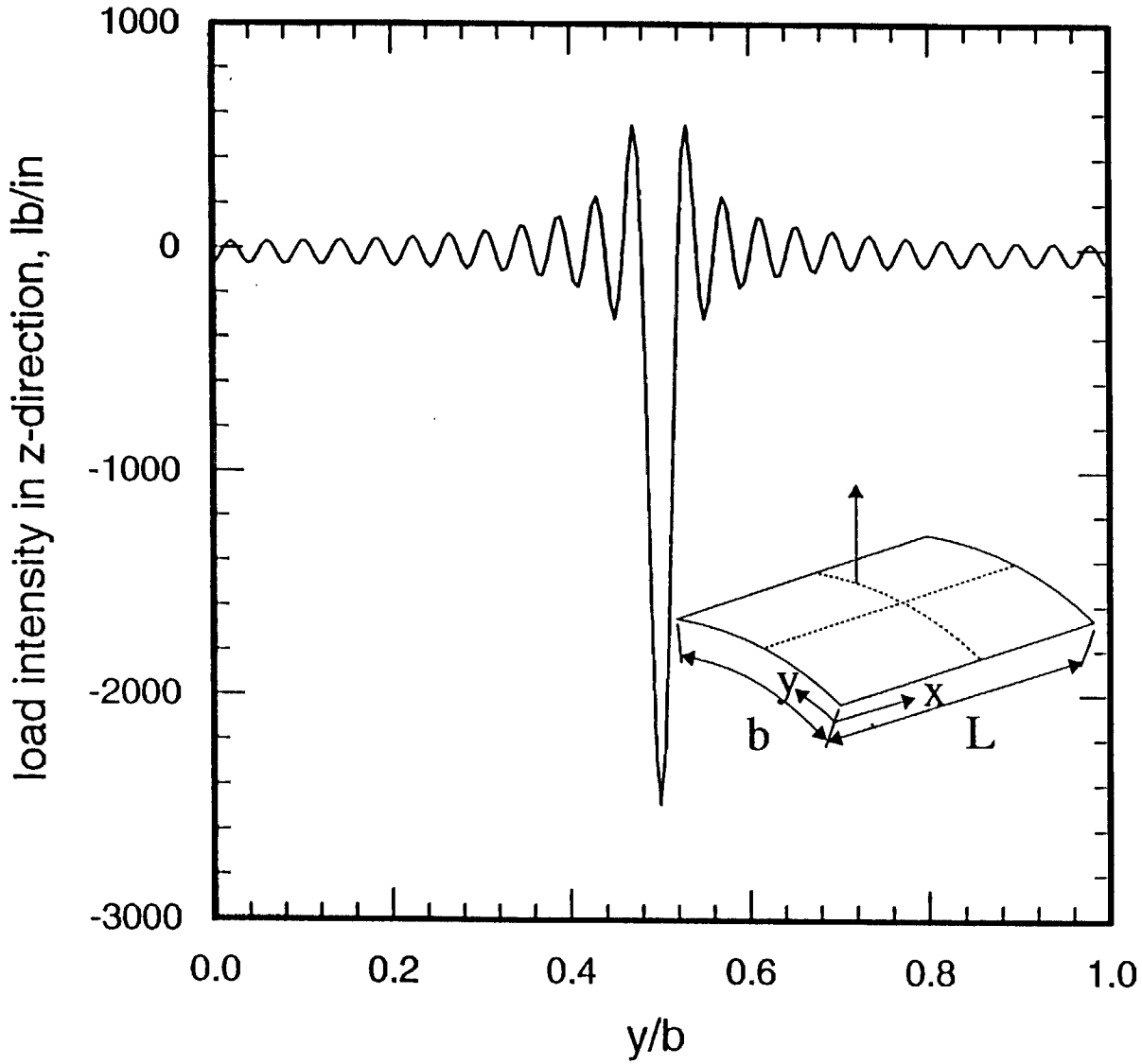

Peak values of the interacting normal loads

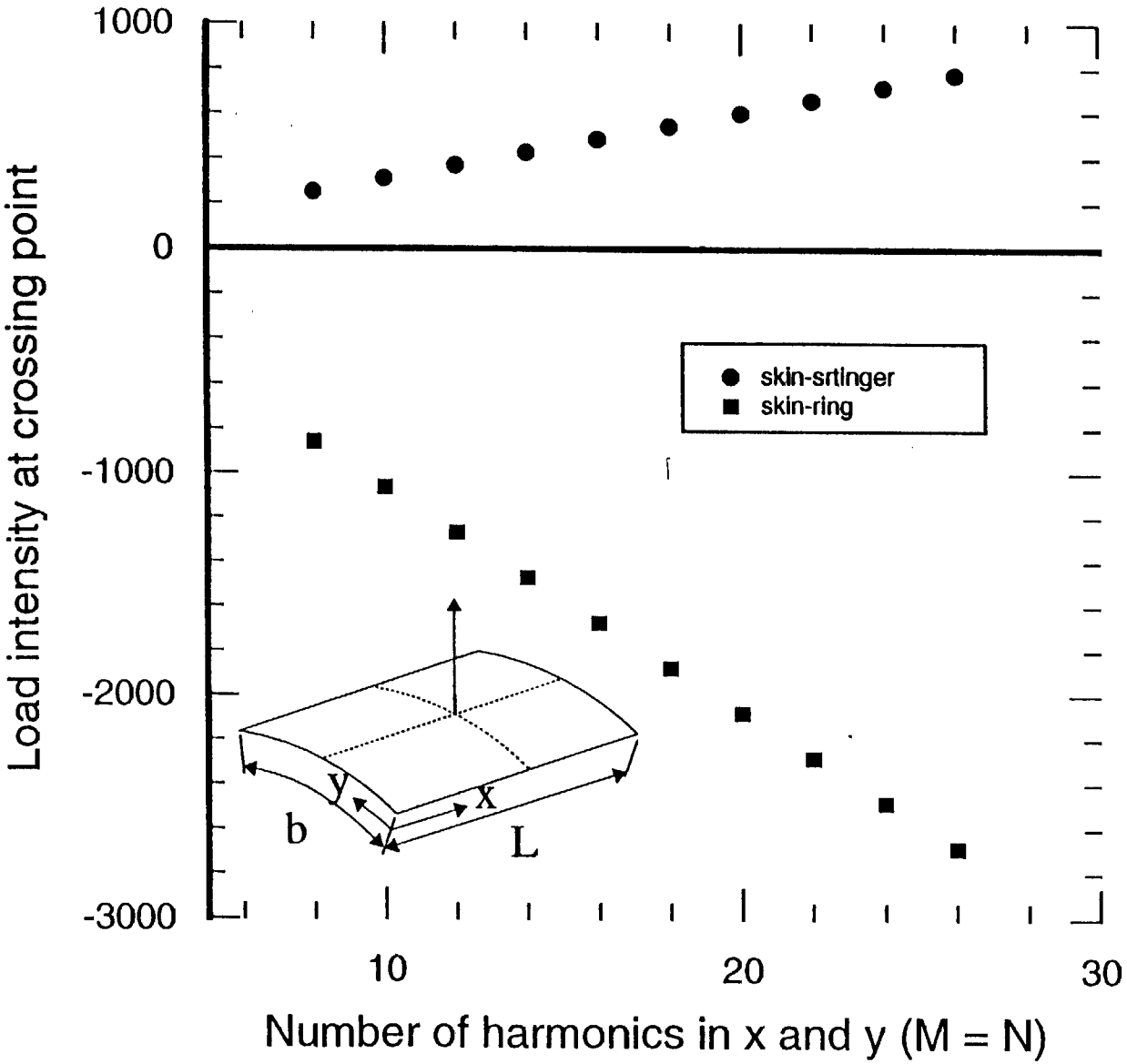

Concluding remarks

- Singular behavior for interacting normal loads at stiffener crossing point.
- Displacements and circumferential normal strains for shell compare very well to those presented by Wang and Hsu.
- The distribution of axial normal strain on the shell surfaces in the circumferential direction do not show a decrease in magnitude at the stringer location. Wang and Hsu results do show this decrease.